

# The Outer Disk of the Milky Way Seen in $\lambda 21$ -cm Absorption

John M. Dickey

*University of Tasmania*

*School of Maths and Physics, Private Bag 37, Hobart, TAS 7001, Australia*

john.dickey@utas.edu.au

Simon Strasser

*University of Minnesota and Dominion Radio Astrophysical Observatory*

B.M. Gaensler

*Institute of Astronomy, School of Physics, The University of Sydney*

Marijke Haverkorn

*NRAO Jansky Fellow, University of California at Berkeley and Astron - Netherlands  
Institute for Radio Astronomy*

Dain Kavars

*University of Minnesota and Ball State University*

N. M. McClure-Griffiths

*Australia Telescope National Facility, CSIRO*

Jeroen Stil, A. R. Taylor

*University of Calgary*

## ABSTRACT

Three recent surveys of 21-cm line emission in the Galactic plane, combining single dish and interferometer observations to achieve resolution of  $1'$  to  $2'$ ,  $\sim 1$  km s $^{-1}$ , and good brightness sensitivity, have provided some 650 absorption spectra with corresponding emission spectra for study of the distribution of warm and cool phase HI in the interstellar medium. These emission-absorption spectrum pairs are used to study the temperature of the interstellar neutral hydrogen in the outer disk of the Milky Way, outside the solar circle, to a radius of 25 kpc.

The cool neutral medium is distributed in radius and height above the plane with very similar parameters to the warm neutral medium. In particular, the ratio of the emission to the absorption, which gives the mean spin temperature of the gas, stays nearly constant with radius to  $\sim 25$  kpc radius. This suggests that the mixture of cool and warm phases is a robust quantity, and that the changes in the interstellar environment do not force the HI into a regime where there is only one temperature allowed. The mixture of atomic gas phases in the outer disk is roughly 15% to 20% cool (40 K to 60 K), the rest warm, corresponding to mean spin temperature  $\sim 250$  to 400 K.

The Galactic warp appears clearly in the absorption data, and other features on the familiar longitude-velocity diagram have analogs in absorption with even higher contrast than for 21-cm emission. In the third and fourth Galactic quadrants the plane is quite flat, in absorption as in emission, in contrast to the strong warp in the first and second quadrants. The scale height of the cool gas is similar to that of the warm gas, and both increase with Galactic radius in the outer disk.

*Subject headings:* ISM: atoms, ISM: clouds, ISM: structure, Galaxy: disk, Galaxy: structure

## 1. Background

Surveys of the Milky Way disk using the 21-cm line have been one of the most powerful means of tracing the structure and properties of the Galaxy for over 50 years (reviewed by Burton 1988, 1991; Lockman 2002; Kalberla and Dedes 2008; Kalberla and Kerp 2009). Our knowledge of the outer Galaxy, beyond the solar circle, is particularly dependent on HI emission surveys, as emission from other species in the interstellar medium (ISM) declines faster with Galactocentric radius,  $R_g$ . Thus the 21-cm line is much easier to detect and to use as an ISM tracer in the outer Galaxy than lines from molecules like CO, both because the atomic phase of the medium is becoming more and more the dominant form of the gas mass with increasing Galactic radius,  $R_g$ , and because the HI has a higher spatial filling factor than the molecules.

Since the pioneering HI surveys of the 1950's it has been clear that the Milky Way disk extends to at least two to three times the radius of the solar circle,  $R_o$ . Surveys covering wide latitude ranges (Burke 1957; Oort, Kerr, and Westerhout 1958) showed that the HI disk in the outer Galaxy is warped: in the longitude range  $50^\circ$  to  $130^\circ$  the middle or centroid of the gas distribution moves toward positive  $z$ , where  $z$  is the height above the plane defined by latitude  $b = 0^\circ$ . In the third and fourth quadrants (longitudes  $240^\circ$  to  $310^\circ$ ) there is

very little displacement of the gas from this flat plane, at least to  $R_g \simeq 25$  kpc. This does not necessarily imply an asymmetry in the Milky Way disk, since our location places us much nearer the warp in the first and second quadrants than its reflection on the other side of the Galactic center, which would be expected at high longitudes in the fourth quadrant (Kalberla et al. 2007; Levine, Blitz, and Heiles 2006). At the same radii where the warp becomes significant,  $R_g \sim 15$  kpc, the gas disk begins to flare, meaning that its scale height increases. This happens at all galactocentric azimuths,  $\phi$ , defined as zero in the direction of longitude zero, i.e. a ray pointing from the Galactic center directly away from the sun.

Although surveys of HI **emission** at low Galactic latitudes have been done for many years and with many telescopes, surveys of **absorption** in the 21-cm line have been much less common, because the instrumental requirements to measure absorption are more stringent than for emission, as discussed in section 2 below. Interferometer and aperture synthesis telescopes like the NRAO Very Large Array (VLA) were used for low latitude absorption surveys in the 1970's and 80's (Radhakrishnan et al. 1972; Goss et al. 1972; Mebold et al. 1982; Dickey et al. 1983; Kolpak et al. 2002), but interferometers have limited capability to measure the 21-cm emission, so surveys of emission and absorption in these decades were done separately using single dish telescopes to measure the emission. This necessarily gave very different effective beam sizes for the emission and absorption spectra, which is problematic for analysis that involves combining the two.

In the late 1990's and early 2000's three large surveys of the 21-cm emission at low latitudes were undertaken: the Canadian Galactic Plane Survey (CGPS, Taylor et al. 2003), the Southern Galactic Plane Survey (SGPS, McClure-Griffiths et al. 2005), and the VLA Galactic Plane Survey (VGPS, Stil et al. 2006). These surveys were the first to combine data from single dish and aperture synthesis telescopes, for the latter applying the recently perfected mosaicing technique (Sault, Staveley-Smith, and Brouw 1996) for recovering the short-spacing information. This allowed maps of the HI to be made over wide areas with sensitivity to all spatial scales, from many degrees down to the survey resolution of  $45''$  (VGPS),  $1'$  (CGPS) or  $2'$  (SGPS). Thus the survey data is equivalent to a fully sampled map made with a single dish telescope with this beamwidth; such a single dish would have to be 500m or more in diameter! This resolution allows reasonably accurate measurement of the absorption spectra toward a large number of continuum background sources at low latitudes, with corresponding emission interpolated from spectra nearby taken with the same resolution. The resulting emission-absorption spectrum pairs are ideally suited for measurement of the excitation of the 21-cm line from interstellar gas throughout the Galactic plane. This paper presents these emission-absorption spectra from the three surveys, and discusses briefly their implications for the thermodynamics of the hydrogen in the outer disk of the Milky Way. A preceding paper in this series (Strasser et al. 2007) presents a preliminary study of the

absorption data from these surveys, and discusses the morphology of the cool gas complexes seen at large  $R_g$ .

The main motivation to measure emission and absorption spectra with the same resolution in the same directions is in order to determine the excitation temperature of the 21-cm line, called the spin temperature,  $T_{sp} = \frac{T_{EM}}{1-e^{-\tau}}$  where  $T_{EM}(v)$  is the brightness temperature of the HI line as a function of radial velocity in the emission spectrum and  $\tau(v)$  is the optical depth of the HI line. In the Galactic environment  $T_{sp}$  is generally close to the kinetic temperature (see Furlanetto, Oh, and Briggs 2006, for a review of the astrophysics of the spin temperature in various environments). Blending of different regions with different temperatures along the line of sight can make the interpretation complicated, as discussed briefly in section 4 below, and more fully by Dickey et al. (2003). Because of this blending of warm and cool gas at the same velocity, the measured value of  $T_{sp}$  is generally higher than the temperature of the cool clouds that are responsible for most of the absorption,  $T_{cool}$ . This bias is independent of distance. Surveys of emission and absorption at low latitudes make it possible to map the spin temperature throughout the Galaxy, using radial velocity as a kinematic distance indicator. In the outer Galaxy this is of particular interest, since the physical processes that dominate heating and cooling in the atomic phase may change drastically with  $R_g$ . Going from the solar circle to  $R_g \simeq 20$  kpc the density of stars in the disk drops by more than an order of magnitude, and the acceleration due the gravity of the disk,  $K_z$ , drops similarly, which is the cause of the flaring or thickening of the gas layer. Although the ISM is not necessarily in hydrodynamic equilibrium with the gravitational potential of the disk on small scales, at least on long time scales the gas pressure cannot be very different from that set by the gravitational force on the gas above (Spitzer 1956). Thus the average pressure at mid-plane must drop by more than an order of magnitude in the outer Galaxy compared to its solar circle value. Depending on the metallicity gradient, the standard theory of HI thermodynamic equilibrium (Wolfire et al. 1995, 2003) could predict that this pressure drop would lead to an overall phase change, with all the cool neutral medium (CNM) converting to warm neutral medium (WNM) at some  $R_g$ . A major result of this study, described in sections 3 and 4, is therefore something of a surprise, as we find that the mixture of CNM and WNM is robust, with little or no change in the relative fractions of these two phases with  $R_g$  out to nearly three times  $R_o$  or 25 kpc.

## 2. Survey Data Reduction

To measure absorption requires a continuum background source, and a way of subtracting the emission of the gas toward the source so that the optical depth can be determined.

Since emission and absorption are mixed in the spectrum toward the background source, an interpolation of the surrounding emission spectra must be used to estimate and subtract the emission at the position of the continuum. The emission at the position of the continuum source is estimated in the following way: 1) The structure of the continuum source is determined from the line free channels. 2) The absorption is determined on source and 3) the expected emission estimated from the close surroundings of the source. Accurate estimates for emission requires a combination of single dish and interferometer data. At low Galactic latitudes the HI emission shows random spatial variations on all angular scales, so a small telescope beam is required in order for this interpolation to be made over angles of a few arc minutes or less. Typically the mean square emission fluctuations on a given angle,  $\theta$ , are proportional to  $\theta^{-3}$  to  $\theta^{-4}$  (Dickey et al. 2001), so the error in the interpolated emission profile depends on the beamwidth to a power between 1.5 and 2. For a given level of error in this interpolated emission spectrum, the resulting error in the absorption ( $1 - e^{-\tau}$ ) goes inversely as the continuum antenna temperature due to the background source. This continuum antenna temperature is given by the source flux density times the telescope gain ( $G$  in K/Jy), which itself is inversely proportional to the square of the beam width. Thus the error in the measured absorption introduced by emission fluctuations decreases with decreasing beam width to a power between three and four. This effect dominates other sources of error such as ordinary radiometer noise in most 21-cm absorption surveys, particularly at low latitudes. For example, the Arecibo telescope, with beamwidth of  $3.2'$ , is able to measure absorption spectra toward continuum sources of a few Jy or stronger at high and intermediate latitudes (Heiles and Troland 2003a), but for latitudes below about  $10^\circ$  even this beam size is too large to give a sufficiently accurate interpolated emission profile.

Absorption spectra may suffer more from emission fluctuations than the emission spectra do, because an error in the interpolated emission that is subtracted from the spectrum toward the continuum source can cause a large fractional error in the optical depth. Aperture synthesis telescopes can solve the problem of fluctuations in the emission by performing a high-pass spatial filtering of the brightness distribution as set by the  $uv$  plane sampling function of the telescope baselines. Thus telescopes like the VLA and the Australia Telescope Compact Array (ATCA) can measure absorption toward compact continuum sources brighter than a few tens of mJy, because the longer baselines of these telescopes are sensitive only to structure smaller than a few arc seconds. This spatial filter can also reduce the continuum emission of the background source, depending on its angular size, so except for the most compact continuum sources there is a point of diminishing returns in the spatial filtering by using longer and longer baselines to measure 21-cm absorption. The SGPS data have been spatially filtered to improve the accuracy of the absorption spectrum (but not for the emission spectrum, of course), the radius of the spatial filter is adjusted to leave the most continuum

while minimizing the spectral line emission that leaks through the spatial filter due to small angle emission variations. The effect of these emission fluctuations in the absorption spectra is obvious because they generate spurious “absorption” lines with a symmetric distribution around zero in  $(1 - e^{-\tau})$ , i.e. equal numbers of spurious negative and positive peaks in the optical depth.

Details of the techniques for doing the interpolation of the emission and so measuring the emission and absorption are given by Strasser and Taylor (2004); Dickey et al. (2003); McClure-Griffiths et al. (2001); Strasser (2006). These techniques are slightly different for the different surveys. For the SGPS and VGPS surveys the continuum was measured together with the spectral line channels, but for the CGPS the continuum was measured separately. So for the CGPS absorption spectra the absolute calibration of the optical depth has some errors in overall scale factor, typically this is less than 5% but in a few cases as high as 10%. Table 1 gives observational parameters of the different surveys. Note that the survey data provided by the web servers on Table 1 have had the continuum subtracted, whereas the analysis described here was necessarily done with data from an earlier stage of the reduction, before the continuum subtraction.

The spectra are grouped according to the continuum antenna temperature of the background source, which sets the noise in  $(1 - e^{-\tau})$ , as measured at frequencies away from the Galactic velocities where there is no emission or absorption in the 21-cm line. For the brightest continuum sources, the noise in  $(1 - e^{-\tau})$  is  $\sigma_\tau \sim 10^{-2}$ . There are 77 spectrum pairs with  $\sigma_\tau < 0.02$  in the three surveys combined. Numbers with  $\sigma_\tau$  below 0.05 and 0.10 are given on table 1. Although the spectra in the third group ( $0.05 < \sigma_\tau < 0.1$ ) are not of high enough quality to measure accurate values for  $T_{sp}$  in each velocity channel, they can give useful results for the integral of  $(1 - e^{-\tau})$  over broader ranges of velocity, particularly when averaged together with others in a sample of many spectra. The critical point is that both for radiometer noise and for errors in the absorption spectra due to fluctuations in the emission, there is no bias toward positive or negative values of  $(1 - e^{-\tau})$ .

The emission and absorption spectrum pairs are shown in figures 1-3, ordered by longitude, for the three groups defined by  $\sigma_\tau \leq 0.02$ ,  $0.02 < \sigma_\tau \leq 0.05$ , and  $0.05 < \sigma_\tau \leq 0.10$ . The print edition shows just the first and last pair for each survey in each group. The left hand panel shows the emission and absorption spectra, with LSR velocity scaled across the bottom, and absorption  $(1 - e^{-\tau})$  scaled on the left hand axis. To provide as much detail as possible in the absorption profile, the velocity scale is expanded to cover only the range where the emission is non-zero, which necessarily includes all the absorption.

The emission spectra (plotted in grey, or in gold on the electronic edition) are offset upward from the absorption spectra for clarity, and scaled in K of brightness temperature

on the right hand axis of the left hand panel, which is the same scale as the vertical axes of the right hand panel. The bottom axis of the right hand panel is again  $(1 - e^{-\tau})$ . Thus the right hand panel shows emission plotted against absorption. These plots are crowded in many cases, but the points on the right panel can be identified with velocity channels on the left panel by drawing a horizontal line through the  $T_{EM}$  axis between the two panels. Analysis of the separate loops on the right hand panel allows the temperature of the cool gas traced by the absorption to be determined, the remaining emission is due to warm gas blended in velocity with the cool gas, some of which may be associated with the cool clouds and some not (Mebold et al. 1997; Dickey et al. 2003). This analysis is beyond the scope of this paper, but it has been performed by Strasser (2006) for all the absorption features in all the spectra.

### 3. Results

#### 3.1. Longitude - Velocity Diagrams

The absorption spectra are necessarily taken where the background sources are, which does not give a regular and fully sampled map of the optical depth. In order to study the Galactic distribution of the cool gas that causes the absorption, we bin the spectra into grids of longitude and velocity as shown on figure 4. These show pairs of longitude-velocity diagrams, using the emission-absorption spectrum pairs, with all spectra contributing to each bin averaged together. The longitude step size is 1.8 degrees and the velocity step size is  $2 \text{ km s}^{-1}$ . Typically, more than one spectrum contributes to each bin. Spectra from the full latitude range of each survey are included.

The longitude-velocity diagrams of the emission (figure 4) are similar to plots from emission surveys (e.g. McClure-Griffiths et al. 2005) which allow structures in the density and velocity distributions of the ISM to be studied in many ways (reviewed by Burton 1988). In this case the relatively sparse sampling provided by the background continuum source directions makes the  $l$ - $v$  diagram appear crude by modern standards, but the major features are clear. Figure 4 shows two versions of each  $l$ - $v$  diagram, with two different grey scales, to make these visible. On the upper panel, curves of constant galactocentric distance,  $R_g$ , are indicated, based on a flat rotation curve outside the solar circle. The flat rotation curve approximation gives simple equations for the kinematic distance,  $d(v)$ , and hence for  $R_g$  and  $\phi$  from the laws of cosines and sines, respectively:

$$\frac{d}{R_0} = \cos \lambda + \sin \lambda \sqrt{\left(\frac{v}{\cos b} + \sin l\right)^{-2} - 1} \quad (1)$$

$$\frac{R_g}{R_0} = \sqrt{1 + d^2 - 2d \cos \lambda} \quad (2)$$

$$\phi = \arcsin\left(\sin \lambda \frac{d}{R_g}\right) \quad (3)$$

where  $d(v)$  is the distance (from the sun) as a function of the observed radial velocity,  $v$ , in units of  $v_o \equiv 220 \text{ km s}^{-1}$ , the LSR velocity around the solar circle (which is assumed to be the circular velocity for all  $R_g > R_0$ ), and  $\lambda$  is equal to the longitude,  $l$ , in the first and second quadrants but  $\lambda = -l$  in the third and fourth quadrants. Here  $d$  and  $R$  are both in units of  $R_o \equiv 8.5 \text{ kpc}$ . Note that  $R_o$  and  $v_o$  are simply scale factors that do not otherwise effect the analysis, and even the choice of a flat rotation curve is not much more significant than a choice of scale. Using any other smooth monotonic function for the circular rotation velocity vs.  $R$  would cause a smooth stretching of the scale of  $R$ , but otherwise the results of the analysis would be unchanged. The upper right panel of figure 4 shows for comparison distances derived from a rotation curve that is flat to 15 kpc and then drops as a Keplerian. This certainly under-estimates the distance to gas at a given radial velocity, but the displacement of the curves is less than  $20 \text{ km s}^{-1}$  compared with those on the top left.

The lower panels of figure 4 show, with different grey scales, the longitude-velocity diagram of  $(1 - e^{-\tau})$ , the optical depth of the 21-cm line. The structures seen in the absorption correspond to structure seen in emission, but with more contrast between arm and interarm regions. This is clear in spite of the higher noise level in the optical depth. This may be partly due to the fact that the linewidths seen in absorption are narrower than those of HI emission lines; typically the full width at half maximum of an absorption line is  $4 \text{ km s}^{-1}$  whereas emission features have widths of 10 to  $20 \text{ km s}^{-1}$ . In addition, the volume filling factor of the CNM that causes the HI absorption is much less than that of the WNM seen in emission, roughly 3 to 5% vs. roughly 50% (Kalberla and Kerp 2009). So for many reasons the HI absorption traces better than the emission the structures seen in cold gas, on large scales as seen on the  $l$ - $v$  diagram as well as on smaller scales in individual spectrum pairs. In this way the 21-cm absorption has some of the characteristics of molecular line tracers such as  $^{12}\text{CO}$  and  $^{13}\text{CO}$  emission (Jackson et al. 2002).

The  $l$ - $v$  diagrams of the emission and absorption are shown in a different format by Strasser et al. (2007, figure 3). Comparison between that technique, which simply plots



the absorption spectra at their respective longitudes with color-coding for the depth of the absorption, with the binning technique used in figure 4 is interesting. In Strasser et al. (2007) the corresponding  $l$ - $v$  diagram of the emission includes all data, not simply the directions toward the background sources used for the absorption, so it has much finer resolution in longitude. As discussed in that paper, absorption surveys provide vital information for tracing large scale features in the outer disk, such as spiral arms.

### 3.2. Radial Distribution of the Opacity

To study the distribution of the CNM on the largest scales in the outer Galaxy, we transform the velocity into distance from the Galactic center using equations 1 - 3, and then average over annuli of constant  $R_g$ . This gives figure 5. On each figure the data from the three surveys is plotted separately. This separates data from the lower longitudes in the first quadrant,  $18^\circ \leq l \leq 65^\circ$  in the VGPS from the higher longitudes in the first and second quadrant,  $65^\circ \leq l \leq 170^\circ$  in the CGPS, and the third and fourth quadrant,  $255^\circ \leq l \leq 357^\circ$  of the SGPS. These are plotted in gold, black, and red respectively on the electronic edition. The x axis of figure 5 shows  $R_g$  ranging from 8.5 to 25 kpc in steps of  $0.1 R_o$  or 0.85 kpc. The y axis on the top panel of figure 5 plots the log (base 10) of the average of the emission brightness temperature (in K), times the spectral channel band width,  $\Delta v$  in  $\text{km s}^{-1}$ , divided by the line of sight path length,  $\Delta L$  in kpc, corresponding to that range of velocity:

$$\left\langle \frac{T_{EM} \Delta v}{L} \right\rangle = \frac{\sum_i T_i \frac{\Delta v}{\Delta L} w_i}{\sum_i w_i} \quad (4)$$

where the sum is taken over many spectra, and many spectral channels,  $i$ , in each spectrum, that correspond to the given range of  $R_g$ , and  $w_i$  is a weight factor set by the inverse of the noise in each absorption spectrum. The path length corresponding to the velocity width of one spectral channel is  $\Delta L = |d(v + \Delta v) - d(v)|$  at the longitude and velocity of channel  $i$ . We experimented with different choices for noise weighting,  $w_i$ , converging on the inverse of the rms noise in  $(1 - e^{-\tau})$  as the most robust. Of course this weighting is designed to optimize the signal to noise of the resulting average only for the **optical depth**, shown on the middle panel of figure 5, but we use the same weighting for the emission so that the two averages can be directly compared with all other parameters kept the same.

The brightness temperature average in equation 4 has units  $\text{K km s}^{-1} \text{kpc}^{-1}$ , but this can be converted to density of HI since the brightness temperature averaged over a velocity step traces the column density of gas (for optically thin 21-cm emission):

$$\left\langle \frac{n_H}{\text{cm}^{-3}} \right\rangle = \frac{N_H}{\Delta L} = 5.9 \cdot 10^{-4} \left\langle \frac{T_{EM} \Delta v}{\text{K km s}^{-1}} \left( \frac{L}{\text{kpc}} \right)^{-1} \right\rangle \quad (5)$$

with  $\Delta L$  the path length interval,  $N_H$  the column density of HI and  $n_H$  the average space density along this path. Thus the value 3 on the y axis of the top panel on figure 5, meaning  $10^3 \text{ K km s}^{-1} \text{ kpc}^{-1}$ , corresponds to density  $0.59 \text{ cm}^{-3}$ , which is roughly the midplane density at the solar circle. The density drops rapidly outside the solar circle, with exponential scale length about 3.1 kpc. This is generally consistent with the much better determined values for these numbers from large scale HI emission surveys (Kalberla and Dedes 2008). The strong departures from a smooth radial decrease in the CGPS and VGPS data on figure 5 are due to a combination of the Perseus arm, which increases the HI density above its mean value at  $R_g \simeq 10$  to 15 kpc in the first and second quadrants, and the warp, that strongly reduces the HI density in the VGPS longitude range at  $R_g > 15$  kpc. The SGPS data show weaker departures from the underlying exponential decrease, because the effects of the warp are much less significant in the third and fourth quadrants.

The middle panel of figure 5 shows the radial variation of the opacity in the HI line, i.e. the absorption equivalent width per unit line of sight length,  $\langle \kappa \rangle$ , which is the major new result of this study. The y axis now plots the average of the absorption,  $(1 - e^{-\tau})$ , per spectral channel, weighted in exactly the same way as for the emission in equation 4, giving the average of the ratio of the density divided by the spin temperature:

$$\left\langle \frac{n_H}{T_{sp}} \right\rangle \left( \frac{\text{K}}{\text{cm}^{-3}} \right) = \left\langle \frac{N_H}{T_{sp}} \frac{1}{L} \right\rangle \left( \frac{\text{K cm}}{\text{cm}^{-2}} \right) = 5.9 \cdot 10^{-4} \left\langle \frac{\tau \Delta v}{\text{km s}^{-1}} \left( \frac{L}{\text{kpc}} \right)^{-1} \right\rangle \quad (6)$$

with the quantities as in equation 5, and  $T_{sp}$  the excitation temperature of the 21-cm transition. The term in brackets in the right hand expression in equation 6 is the opacity,  $\langle \kappa \rangle$ , where the brackets denote a line of sight average over all phases of the ISM. In this analysis we work with the directly observed quantity  $(1 - e^{-\tau})$  rather than  $\tau$ , so that the noise is not amplified at velocities where the optical depth is significant, this substitution causes the values to be slight underestimates. This is not significant in the outer Galaxy where the optical depth is generally much less than one. On the y axis of the middle panel of figure 5, the value 1, meaning  $\langle \kappa \rangle = 10^1 \text{ km s}^{-1} \text{ kpc}^{-1}$ , now corresponds to, e.g., density  $0.59 \text{ cm}^{-3}$  and spin temperature 100 K. The average of  $T_{sp}$  over WNM and CNM at the solar circle is between 150 and 250 K (Dickey et al. 2000), so the expected value for  $\frac{n}{T_{sp}}$  is about  $3 \cdot 10^{-3} \text{ cm}^{-3} \text{ K}^{-1}$ , corresponding to 0.7 on the left-hand axis of figure 5, middle panel. Absorption surveys of the inner Galaxy typically give numbers of 5 to  $10 \text{ km s}^{-1} \text{ kpc}^{-1}$  for  $\langle \kappa \rangle$ , which is

consistent with the data from the three surveys at the left edge of the middle panel of figure 5 (Kolpak et al. 2002; Garwood and Dickey 1989).

The radial distributions of the emission and the absorption can be combined into an effective spin temperature by dividing the azimuthal averages of the emission brightness temperature per unit line of sight distance, shown on the top panel of figure 5, by the optical depth per unit distance shown on the middle panel. The result is shown on the bottom panel. The y axis now is the average excitation temperature, computed not by dividing the emission by the absorption channel-by-channel, but by dividing the averages of many channels from many spectra that fall in the same radial bins. The result is surprisingly constant with Galactic radius. Whereas the emission and absorption alone decrease by some two orders of magnitude over the radial range 10 to 25 kpc, including departures from the smooth exponential by at least a factor of three at certain longitudes, yet their ratio stays constant within a factor of two over this entire radial range, with the exception of the VGPS at  $R_g > 17$  kpc, for which the optical depths are so small, due to the warp displacing the plane out of the survey area, that the absorption is not detected above the noise in this survey at these radii.

On the bottom panel of figure 5 the SGPS and VGPS show very good agreement with  $\langle T_{sp} \rangle \simeq 400$  K for  $10 \leq R_g \leq 17$  kpc. The CGPS shows significantly cooler values of  $\langle T_{sp} \rangle \simeq 250$  K over the same range. It is possible that this is due to the geometry of the warp, or some other factor that makes the CNM more abundant in the CGPS area than in the areas covered by the other surveys. It may also reflect in part a bias in the continuum estimate used to compute the optical depth in the CGPS survey, that could arise from the separate processing of the spectral line and continuum images in that survey. For this reason, the absolute calibration of the absorption spectra from the VGPS and SGPS is probably more reliable than that of the CGPS, even though there are many more lines of sight sampled in the CGPS, which leads to smaller error bars on the lower two panels of figure 5.

In all three panels of figure 5 the error bars represent the rms dispersion of the results for the three groups of spectra, those with  $\sigma_\tau < 0.02$ , those with  $0.02 \leq \sigma_\tau < 0.05$ , and those with  $0.05 \leq \sigma_\tau < 0.1$ , averaged without weighting by  $\sigma_\tau$ . The small symbols mark the weighted average of all spectra from all three groups.

### 3.3. Variation of the Opacity with Azimuth, $\phi$

The radial distribution of the HI opacity,  $\langle \kappa \rangle$ , shows broad general agreement among the surveys, but the effect of the warp is clearly quite significant in the VGPS longitude

range, and in the lower longitudes of the CGPS as well. To see this better, we bin the data in radius and azimuth, as shown in figures 6a and 6b. Here the disk is plotted as seen face-on from above the North Galactic Pole. The blank circle at the centre has radius  $R_0$ , and the maximum radius plotted is  $R_g = 25$  kpc. These figures show in grey-scale the same quantities plotted on the y-axis of the upper two panels of figures 5, i.e. the log of the 21-cm emission per unit path length, proportional to  $n_H$ , and the log of the 21-cm absorption per unit path length, proportional to  $\frac{n_H}{T_{sp}}$ . The grey scale extends over a range of  $\sim 10^3$  in each quantity, slightly less than the full scale on the y-axes of the upper two panels on figure 5. The effect of the warp in the first and second quadrants is seen as the white boxes in the lower right corners of each figure.

The azimuthal bins on figures 6a and 6b are ten degrees in angle by 0.1 times  $R_0$  in radius. Even with this relatively coarse sampling, the number of lines of sight passing through some bins is not very large, so there is quite a bit of fluctuation from bin to bin, due to small number statistics. The overall radial trend shown on figure 5 is clearly evident, as is the Perseus Arm in the first and second quadrant, which doubles both the HI density and opacity. In the third and fourth quadrant there is weak indication of the distant arm mapped in 21-cm emission by McClure-Griffiths et al. (2004).

### 3.4. Variation with Height Above the Plane, $z$

Figures 7a and 7b show the dependance of the HI density and opacity on  $z$ , the height above or below the plane defined by  $b=0^\circ$ . In order to have a sufficiently large number of measurements contributing to each 100 pc wide interval in  $z$ , the data in these figures are averaged over ranges in azimuth and radius. Figure 7a shows a histogram of the distribution of the density of HI from equations 4 and 5, as a function of  $z$  over the range  $-1.1 < z < +1.1$  kpc. The different panels show averages over separate regions of  $R_g$  and  $\phi$ , with the top row using only data with  $0^\circ \leq \phi < 100^\circ$ , the middle row using only data with  $100^\circ \leq \phi < 180^\circ$ , and the bottom row using only data with  $180^\circ \leq \phi < 360^\circ$ . The data is also separated into four radial ranges, corresponding to the four columns. The left column uses data from the range  $1.0 < \frac{R_g}{R_0} \leq 1.2$  the next uses data from the range  $1.2 < \frac{R_g}{R_0} \leq 1.4$  the next uses data from the range  $1.4 < \frac{R_g}{R_0} \leq 2.0$  and the right column uses data from the range  $2.0 < \frac{R_g}{R_0} \leq 3.0$ . Figure 7b shows the distribution of  $\langle \kappa \rangle$ , the mean opacity in equation 6, for the same ranges of  $\phi$  and  $R_g$ .

The histograms on figures 7a and 7b indicate the relative amounts of gas at each height,  $z$ , in each region. They are all normalized so that the largest bar has value 1.0. The empty boxes, drawn in red in the on-line edition, indicate that the number of measurements in that

bin is zero, or too small to give a reliable average. Note that the absolute scale is such that the sum of the histograms in each column would match the corresponding radial averages on figures 5, thus the scale expands by a factor of  $\sim 30$  going from the left column to the right column. The rightmost column shows the effects of noise in the optical depth, as there are several negative histogram bars as well as positive ones.

The shapes of the histograms in corresponding panels of figures 7a and 7b show a strong similarity, meaning that the distributions of the emission, proportional to  $n_H$ , and of the opacity, proportional to  $\frac{n_H}{T_{sp}}$ , are very similar. This is surprising, since at the solar circle and in the inner Galaxy the scale height of the CNM is smaller than that of the WNM (Dickey and Lockman 1990; McClure-Griffiths and Dickey 2007). The implication is that the flaring or thickening of the disk in  $z$  as  $R_g$  increases in the outer galaxy, that makes the widths of the distributions increase going from left to right on figures 7a and 7b, is a process that affects the WNM and CNM with equal strength. As Liszt (1983) shows, some of the warm phase gas must be associated with the cool gas, while some is in a more widely spread, neutral intercloud medium. The fact that the scale height of the absorption is only slightly smaller than that of the emission in the outer Galaxy suggests that the scale heights of these two warm HI components are not very different.

The effect of the warp is seen strongly in the top row of panels in both figures 7a and 7b. The first moment or mean value of  $z$  increases with  $R_g$ , finally moving out of the survey window altogether for  $R_g > 15$  kpc. This is the same effect that causes the empty bins in the lower right area of figures 6a and 6b. In the SGPS data, shown in the bottom row of panels on figures 7a and 7b, there is very little departure from the midplane in the averages over  $180^\circ < \phi < 360^\circ$ .

#### 4. Conclusions

The constancy of the mean spin temperature with Galactic radius from  $R_0$  to  $3 \times R_0$ , as shown on the bottom panel of figure 5, indicates that the mixture of CNM and WNM is roughly the same throughout the outer Milky Way disk. This is surprising, given that the physical conditions, in particular the gas pressure, the supernova rate, the radiation field, and the heavy element abundance, are all decreasing with  $R_g$ , and these variations must influence the balance of heating and cooling that determines the thermal phases of the HI.

The mean spin temperature should be interpreted not as a physical temperature, but as a parameter that measures of the mixture of WNM and CNM. This is because the kinetic temperature in the HI varies over a very wide range, from 20 K to  $10^4$  K (Kulkarni and

Heiles 1988). Blending of warm and cool gas at the same velocity along the line of sight to a background source gives a density-weighted harmonic mean of this quantity,

$$\langle T_{sp} \rangle = \frac{T_{EM}}{(1 - e^{-\tau})} = \frac{\int n ds}{\int \frac{n}{T_{kin}} ds} \quad (7)$$

where the integrals in the third expression are taken along the line(s) of sight,  $s$ , including only gas with radial velocity that places it into a given velocity channel or range of channels. Making the assumption that the CNM temperature is roughly constant at some typical value  $T_{cool}$ , and that the WNM temperature is high enough that it does not contribute to the optical depth in the denominator of equation 7, gives

$$\langle T_{sp} \rangle = T_{cool} \frac{n_{WNM} + n_{CNM}}{n_{CNM}} \quad (8)$$

where the ratio of CNM density to total HI (WNM plus CNM) density in this two-phase approximation can be denoted  $f_c = \frac{n_{CNM}}{n_{WNM} + n_{CNM}} = 1 - f_w$  (Dickey et al. 2000). Detailed fitting of the line profile shapes for corresponding features in the emission and absorption spectra can give a good estimate for the CNM temperatures,  $T_{cool}$ , which typically vary between 20 K and 100 K for distinct absorption lines with peak optical depths of 0.1 or higher. The mean value for  $T_{cool}$  is about 50 K, as measured by different techniques in different surveys with different telescopes (Heiles and Troland 2003b; Dickey et al. 2003). Similar analysis by Strasser (2006) of the absorption lines in the CGPS suggests that  $T_{cool}$  does not change significantly or systematically with increasing  $R_g$ . The constancy of  $T_{sp}$  with  $R_g$  thus shows that  $f_c$  is also roughly constant in the outer Galactic disk. Since the bottom panel of figure 5 shows a value of  $\sim 400$  K from the SGPS data from 12 to 25 kpc in  $R_g$ , this gives  $f_c$  in the range 10% to 25% for  $T_{cool}=40$  K to 100 K.

This invariance of  $f_c$  with  $R_g$  is surprising in comparison with the apparently strong variation of  $f_c$  with  $z$  in the inner Galaxy. The CNM and WNM seem to have quite different distributions in  $z$ , with the WNM density showing a long tail reaching to  $|z| \sim 1$  kpc (Lockman and Gehman 1991), while the CNM has scale height of only 100 to 150 pc (Crovisier 1978, Malhotra 1995, but see Stanimirović et al. 2006 and Pidopryhora, Lockman, and Shields 2007 for studies of HI clouds, at heights of 0.5 to 1 kpc in  $z$ , that contain significant amounts of CNM). The difference in these scale heights has been explained by variation in the gas pressure with  $z$ , which shifts the equilibrium values of  $n$  and  $T_{cool}$  for which the total heating and cooling rates are equal (Wolfire et al. 2003).

One way to understand the difference between CNM scale heights in the inner and outer Galaxy is to identify a part of the CNM in the inner Galaxy with the molecular cloud

population. The molecular clouds are the dominant form of ISM mass in the inner Milky Way, particularly in the molecular ring  $3 < R_g < 6$  kpc. In the outer disk the molecular phase makes only a small contribution to the total ISM mass, with the neutral and ionized phases playing the dominant role. The molecular clouds certainly have a different distribution from the atomic gas, with the scale height of the disk being much narrower as traced in CO than in HI, for example. Molecular gas is usually surrounded by and/or mixed with partially atomic gas which shows 21-cm absorption and so appears as CNM (Goldsmith, Li, and Krčo 2007). Molecular line cooling is so efficient that the HI gas in a molecular cloud is cooler than in the atomic-only CNM ( $\sim 20$  K vs.  $\sim 50$  K, Goldsmith 2001), thus molecular clouds contribute disproportionately (compared to their HI column density) to 21-cm absorption surveys of the inner Galaxy (Kalberla and Kerp 2009, section 5). In the outer Galaxy this source of 21-cm absorption is insignificant, so  $f_c$  shows the mixing-ratio of CNM to WNM without confusion by HI in molecular clouds. In the outer disk the evidence on figures 7a-7c suggests that the scale heights of the WNM and CNM are nearly the same.

A more profound question is how the CNM can coexist with the WNM as a familiar two-phase medium, in an environment where the gas pressure, set by the depth of the disk potential and the overburden of gas at higher  $z$ , is as low as it must be in the far outer Galaxy. We see from figure 5 that the density at  $R_g \sim 20$  to 25 kpc is a factor of nearly 100 smaller than at the solar circle, and since the temperatures are similar this means that the gas pressure is less than  $100 \text{ cm}^{-3} \text{ K}$ . The lowest value of the gas pressure that allows the cool phase to exist, even in the environment of the outer disk studied by Wolfire et al. (2003), is  $\sim 250$  to  $300 \text{ cm}^{-3} \text{ K}$ . Supplementing the pressure of the gas with other forms such as magnetic pressure does not necessarily help, since it is the collision rate that sets the cooling in the equilibrium calculation, and so heating-cooling equilibrium is set by product of the density and random velocity, not by the total pressure.

A similar theoretical problem is posed by cool HI clouds in the Magellanic Bridge and in the far outskirts of the Magellanic Clouds (Kobulnicky and Dickey 1999), and in many examples of HI absorption beyond the edges of the disks of other galaxies. Probably the explanation in most cases is that the local space density,  $n_H$ , is increased by an order of magnitude or more above the average,  $\langle n_H \rangle$ , due to shocks, either from supernova explosions or from converging large scale gas flows ultimately driven by gravity. The supernova rate is undoubtedly very low in this environment, but converging flows may be common. As long as the cooling time of the HI is shorter than the dynamical time scale of the large structures on the edges of the Milky Way and other galaxies, the HI may be driven from warm to cool and back to warm as the pressure responds to the larger scale gas dynamics.

As Strasser et al. (2007) show, the spatial distribution of the gas causing the absorption

in the outer Galaxy is not random; the CNM is gathered in large, coherent structures that in turn follow patterns on the  $l$ - $v$  diagram that may connect to the spiral arms of the inner Galaxy. This suggests that departures from circular rotation caused by gravitational perturbations initiate the runaway cooling that precipitates the cool, atomic gas out of the WNM.

A powerful probe of the gas in and around galaxies at high and intermediate redshifts is 21-cm absorption (reviewed by Carilli 2006). An important question in interpreting such lines is how to translate the measured optical depth to HI column density. The results of this study suggest that using a value for  $T_{sp}$  of 250 to 400 K would be appropriate for the Milky Way seen at an impact parameter of 10 to 25 kpc. This is significantly higher than the values of 100 to 150 K often used on the basis of the relative abundances of CNM and WNM inside the solar circle.

We are grateful to F. J. Lockman, P. M. W. Kalberla, and an anonymous referee for helpful suggestions. This research was supported in part by NSF grant AST-0307603 to the University of Minnesota. The Dominion Radio Astrophysical Observatory is operated as a national facility by the National Research Council of Canada. The Canadian Galactic Plane Survey is supported by a grant from the National Sciences and Engineering Research Council of Canada. The National Radio Astronomy Observatory is a facility of the National Science Foundation operated under cooperative agreement by Associated Universities, Inc. The ATCA and the Parkes Radio Telescope are part of the Australia Telescope, which is funded by the Commonwealth of Australia for operation as a National Facility managed by CSIRO.

## REFERENCES

- Burke, B.F., 1957, AJ 62, 90.
- Burton, W.B., 1988, in Galactic and Extragalactic Radio Astronomy, 2nd ed., eds. G.L. Verschuur and K. Kellerman, (New York : Springer-Verlag) p. 295.
- Burton, W.B., 1991, in **The Galactic Interstellar Medium**, Saas-Fe Advanced Course 21, eds. P. Bartholdi and D. Pfenninger [Berlin: Springer-Verlag] section 2.3, pp. 20-22.
- Carilli, C.L., 2006, New A Rev. 50, 162.
- Crovisier, J. 1978, A&A 70, 43.



- Dickey, J.M., Kulkarni, S.R., Heiles, C.E., and van Gorkom, J.H., 1983, ApJS 53, 591.
- Dickey, J.M. and Lockman, F.J., 1990, ARA&A 28, 215.
- Dickey, J.M., Mebold, U., Stanimirović, S., and Staveley-Smith, L. 2000 ApJ 536, 756
- Dickey, J.M., McClure-Griffiths, N.M., Stanimirović, S., Gaensler, B.M., Green, A.J., 2001, ApJ 561, 264.
- Dickey, J.M., McClure-Griffiths, N., Gaensler, B., Green, A., 2003, ApJ 585, 801.
- Furlanetto, S.R., Oh, S.P., and Briggs, F.H., 2006, Physics Reports, 433, 181.
- Garwood, R.W. and Dickey, J.M. 1989, ApJ 338, 841.
- Goldsmith, P.F. 2001, ApJ 557, 736.
- Goldsmith, P.F., Li, D., and Krčo, M., 2007, ApJ 654, 273.
- Goss, W.M., Radhakrishnan, V., Brooks, J.W., and Murray, J.D., 1972, ApJS 24, 123.
- Heiles, C. & Troland, T.H. 2003a ApJS 145, 329.
- Heiles, C. & Troland, T.H. 2003b ApJ 586, 1067.
- Jackson, J.M., Bania, T.M., Simon, R., Kolpak, M., Clemens, D., Hayer, M., 2002, ApJ 566, 81.
- Kalberla, P.M.W., Dedes, L., Kerp, J., and Haud, U., 2007, A&A 469, 511.
- Kalberla, P.M.W. and Dedes, L. 2008, A&A 487, 951.
- Kalberla, P.M.W. and Kerp, J. 2009, ARA&A47, in press.
- Kobulnicky, H.A. and Dickey, J.M., 1999, AJ 117, 908.
- Kolpak, M. A., Jackson, J.M., Bania, T.M., and Dickey, J.M., 2002, ApJ 578, 868.
- Kulkarni, S.R. and Heiles, C., 1988, in Galactic and Extragalactic Radio Astronomy, 2nd ed., eds. G.L. Verschuur and K. Kellerman, (New York : Springer-Verlag) p. 95.
- Levine, E.S., Blitz, L., and Heiles, C., 2006, ApJ 643, 881.
- Liszt, H.S., 1983, ApJ 275, 163.
- Lockman, F.J. and Gehman, C., 1991, ApJ 382, 182.

- Lockman, F.J., 2002, in **Seeing Through the Dust: The Detection of HI and the Exploration of the ISM in Galaxies**, ASP Conference Proceedings, Vol. 276, eds. A.R. Taylor, T.L. Landecker, and A.G. Willis, [San Francisco, Astronomical Society of the Pacific] p. 107.
- Malhotra, S. 1995, ApJ 448, 138.
- McClure-Griffiths, N.M., Green, A.J., Dickey, J.M., Gaensler, B.M., Haynes, R.F., Wieringa, M.H., 2001, PASA 18, 84.
- McClure-Griffiths, N.M., Dickey, J.M., Gaensler, B.M., & Green, A.J., 2004 ApJ 607, L127.
- McClure-Griffiths, N.M., Dickey, J.M., Gaensler, B.M., Green, A.J., Haverkorn, M., & Strasser, S. 2005 ApJS 158, 178.
- McClure-Griffiths, N.M. and Dickey, J.M., 2007, ApJ 671, 427.
- Mebold, U., Winnberg, A., Kalberla, P.M.W., and Goss, W.M., 1982, A&A 115, 223.
- Mebold, U., Dusterberg, C., Dickey, J.M., Staveley-Smith, L., Kalberla, P., Muller, H., and Osterberg, J., 1997, ApJ 490, L65.
- Oort, J.H., Kerr, F.J., and Westerhout, G., 1958, MNRAS 118, 379.
- Pidopryhora, Y., Lockman, F.J., and Shields, J.C., 2007, ApJ 656, 928.
- Radhakrishnan, V., Goss, W.M., Murray, J.D., and Brooks, J.W., 1972, ApJS 24, 99.
- Sault, R.J., Staveley-Smith, L., and Brouw, W.N., 1996, A&AS 120, 375.
- Spitzer, L., 1956, ApJ 124, 20.
- Stil, J.M., Taylor, A.R., Dickey, J.M., Kavars, D.W., Martin, P.G., Rothwell, T.A., Boothroyd, A.I., Lockman, F.J., and McClure-Griffiths, N.M., 2006, AJ 132, 1158.
- Stanimirović, S., Putman, M., Heiles, C., Peek, J.E.G., Goldsmith, P.F., et al. 2006, ApJ 653, 1210.
- Strasser, S. and Taylor, A.R., 2004, ApJ 603, 560.
- Strasser, S.T. 2006 Ph. D. Thesis, University of Minnesota.
- Strasser, S.T., Dickey, J.M., Taylor, A.R., Boothroyd, A.I., Gaensler, B.M., Green, A.J., Kavars, D.W., Lockman, Felix J., Martin, P.G., McClure-Griffiths, N.M., Rothwell, T.A., and Stil, J.M. 2007, AJ 134, 2252.

Taylor, A.R., Gibson, S.J., Peracaula, M., Martin, P.G., Landecker, T.L. et al. 2003 AJ 125, 3145.

Wolfire, M.G., Hollenbach, D., McKee, C.F., Tielens, A.G.G.M., and Bakes, E.L.O., 1995, ApJ443, 152.

Wolfire, M.G., McKee, C.F., Hollenbach, D., and Tielens, A.G.G.M., 2003, ApJ 587, 278.

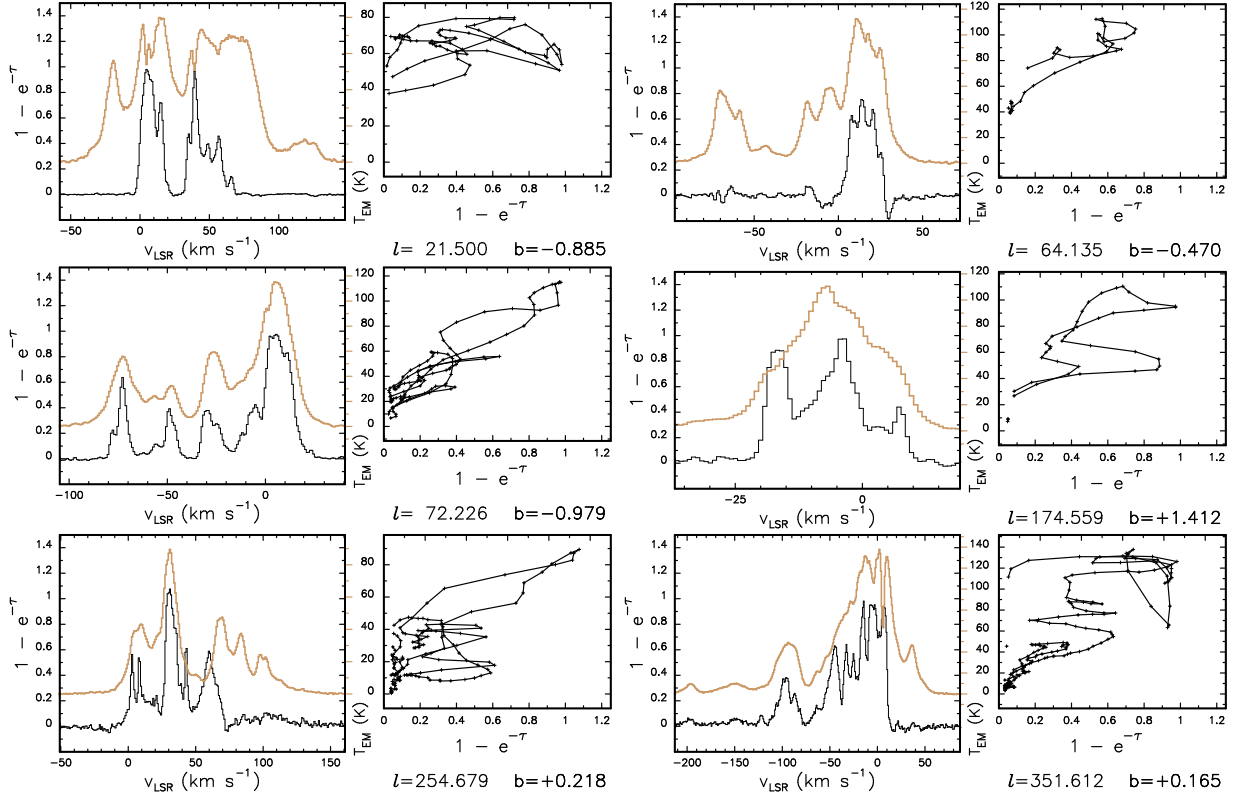


Fig. 1.— Sample spectra from the three surveys with  $\sigma_\tau < 0.02$ . Top row shows the first and last spectrum in this group from the VGPS, the middle row shows the first and last spectrum in this group from the CGPS, and the bottom row shows the first and last spectrum in this group from the SGPS. The left panel shows the absorption spectrum plotted as  $(1 - e^{-\tau})$ , with the corresponding vertical scale on the left, and the emission spectrum,  $T_{EM}$ , offset up and scaled on the right hand axis, between the two panels. In the electronic edition the emission is shown in gold. The right hand panel shows the emission plotted vs. the absorption, with the y axis again the scale for  $T_{EM}$ , and the x axis the scale for  $(1 - e^{-\tau})$ . In the electronic edition all spectra are included, from all three surveys. In the electronic edition figure 1 includes 15 pairs of spectra from the VGPS, 32 from the CGPS, and 30 from the SGPS.

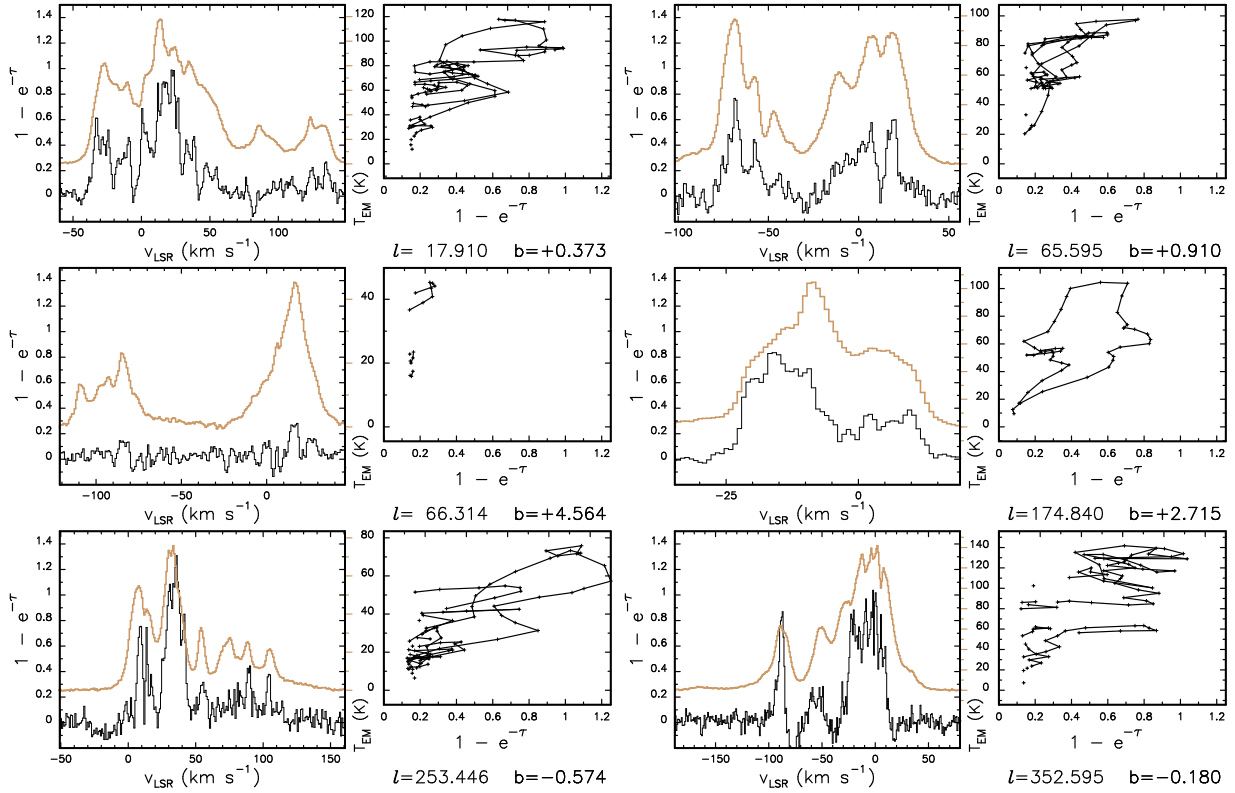


Fig. 2.— Sample spectra from the three surveys with  $0.02 \leq \sigma_\tau < 0.05$ . The layouts of the panels are the same as in figure 1, with the first and last spectra from the VGPS on the top line, the first and last from the CGPS on the second line, and the first and last of the SGPS on the third line. In the electronic edition figure 2 includes 64 pairs of spectra from the VGPS, 108 from the CGPS, and 42 from the SGPS.

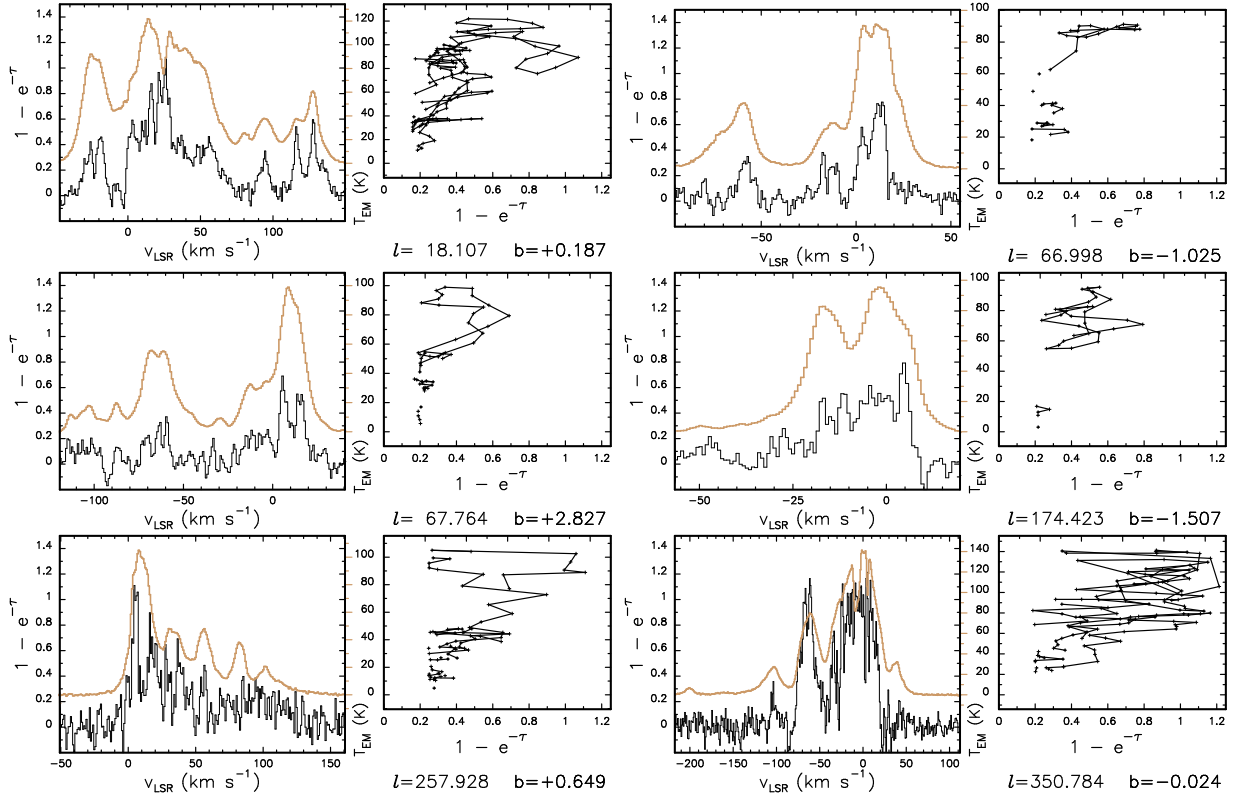


Fig. 3.— Sample spectra from the three surveys with  $0.05 \leq \sigma_\tau < 0.10$ . The layouts of the panels are the same as in figure 1, with the first and last spectra from the VGPS on the top line, the first and last from the CGPS on the second line, and the first and last of the SGPS on the third line. In the electronic edition figure 3 includes 64 pairs of spectra from the VGPS, 108 from the CGPS, and 42 from the SGPS.

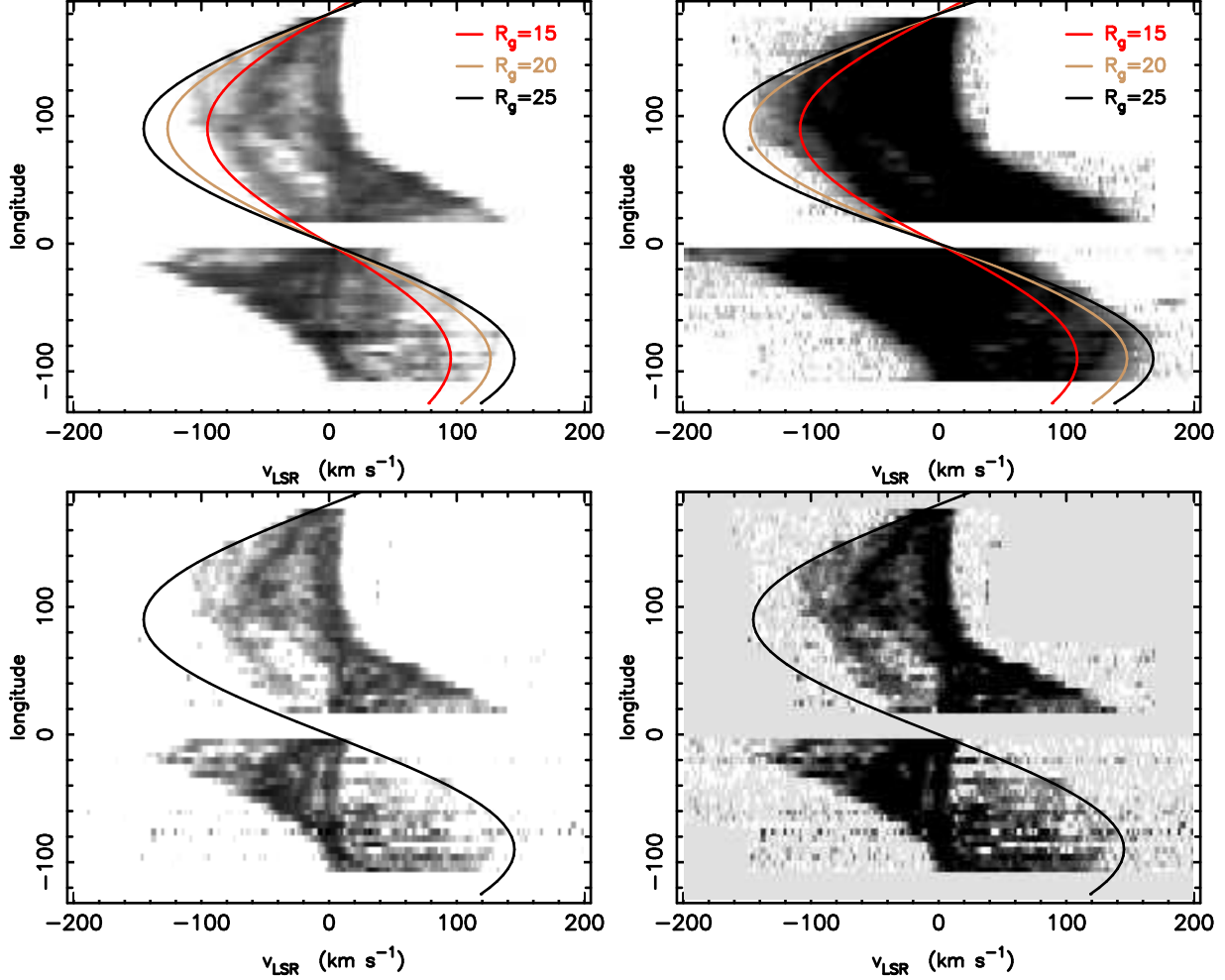


Fig. 4.— Longitude-velocity diagrams for emission,  $T_{EM}$ , and absorption,  $(1 - e^{-\tau})$ . The upper panels show the emission, with two different levels of grey scale. The lower panels show the absorption. The upper panels have lines of constant  $R_g$  indicated. The left panel has the prediction of the flat rotation curve used here (equations 1 - 3), the right panel shows similar curves for a rotation curve that stays flat to 15 kpc and then decreases as a Keplerian. The left hand panels have a shallower grey-scale transfer function than the right hand panels, to better show the structure at different levels. The lower panels have the curve for  $R_g=25$  kpc from the flat rotation curve repeated from the upper left panel.

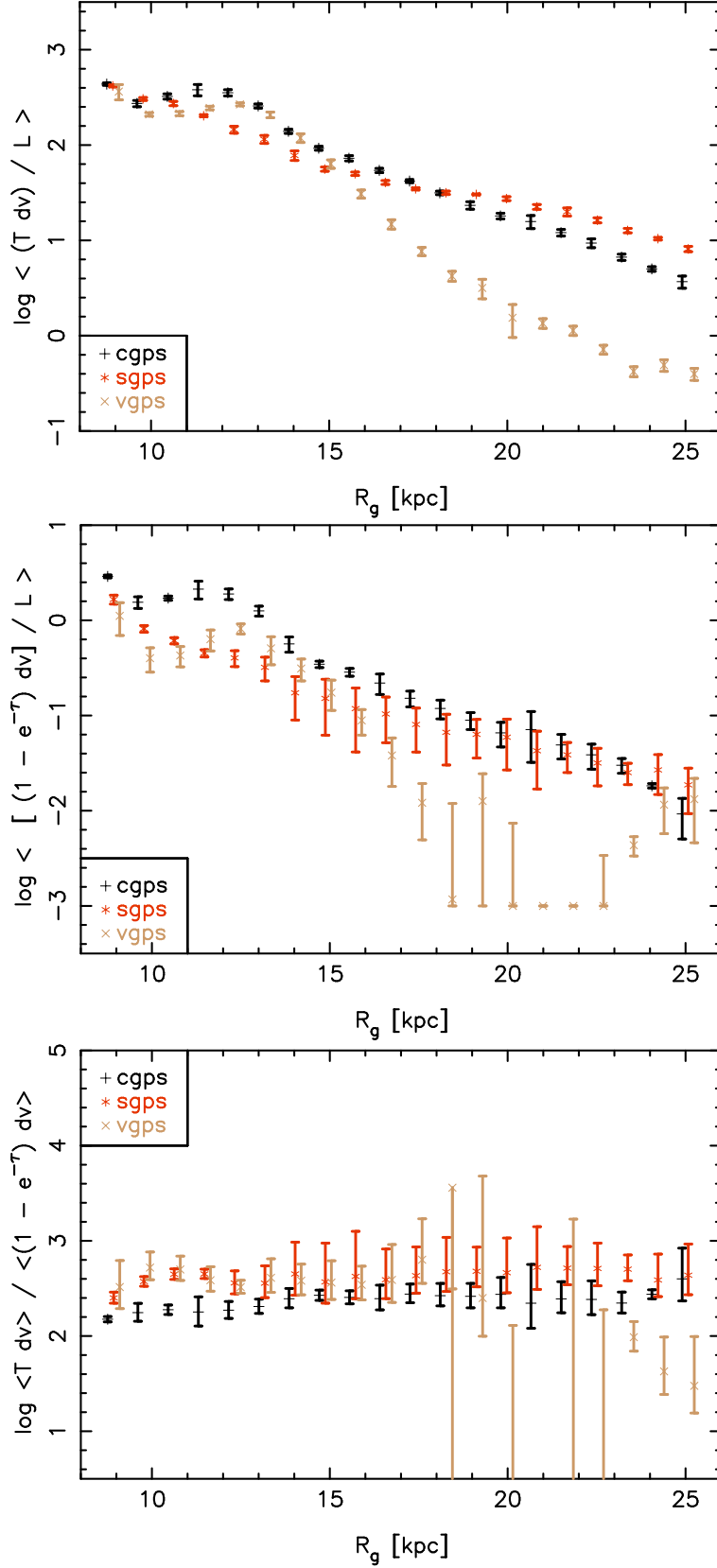


Fig. 5.— The radial dependence of the 21-cm emission per unit path length (top panel, proportional to  $\langle n_H \rangle$ ), the 21-cm absorption per unit path length ( $\langle \kappa \rangle$ , middle panel), and the ratio of emission to absorption, ( $T_{sp}$ , bottom panel).



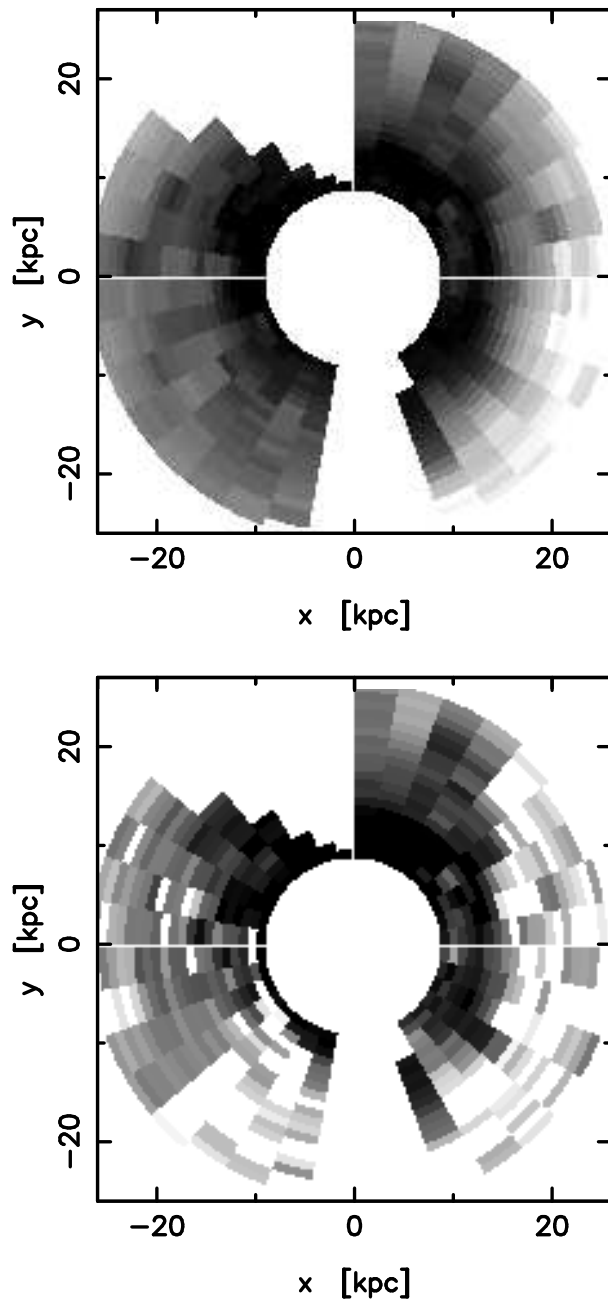


Fig. 6.— The azimuthal distribution of the emission, shown on the upper panel (a), and the opacity shown on the lower panel (b). The effect of the warp is evident in the empty region in the lower right. The Perseus Arm is clearly visible in the first and second quadrants as the dark feature just outside the solar circle. The grey scale is logarithmic, with range +2.5 (black) to -0.5 (white) in the upper panel, and 0 to -2.5 in the lower panel, with units as in the upper two panels of figure 5. The axes are labelled in kpc, assuming  $R_o = 8.5$  kpc.

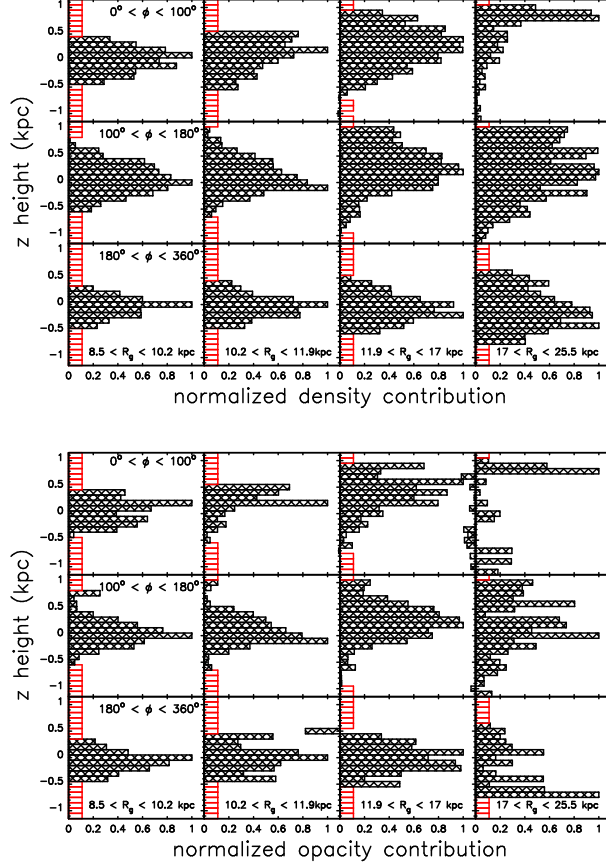


Fig. 7.— Histograms of the distributions of HI density and opacity with  $z$  in different regions of the outer Milky Way disk. The shaded rectangles are histograms, rotated so that the  $z$  axis is vertical, where the height of each bar represents the amount of gas in each 100 pc wide bin in  $z$ , from  $-1.1$  to  $+1.1$  kpc. The unshaded rectangles (red in the electronic edition) mark regions where the number of samples is too small to give reliable results. The different panels contain data from separate regions, with the rows showing different ranges of azimuth,  $\phi$ , and the columns showing different ranges of Galactic radius,  $R_g$ , as indicated. The upper figure (a) shows the distribution of HI density, measured by the emission per unit path length, and the lower panel (b) shows the opacity,  $\langle \kappa \rangle$ . The flaring of the disk is evident as a widening of the distributions with increasing  $R_g$  at all azimuths. The warp is most clearly seen in the top row, as the median  $z$  increases with increasing  $R_g$  in both the emission and the absorption. In all the panels the histograms have been scaled so that the largest bar has unit height. This means that the rightmost column has scale factor more than 30 times larger than the leftmost column in absolute units.

Table 1. Galactic Plane Survey Parameters

Survey	area	angular resolution	velocity resolution	rms noise in $T_{EM}$	Number of Absorption Spectra with $\sigma_\tau$		
					<0.02	0.02-0.05	0.05-0.1
VGPS <sup>a</sup>	$18^\circ < l < 67^\circ$ $-1.3^\circ < b < +1.3^\circ$	1'	1.56 km/s	2K	15	64	49
CGPS <sup>a</sup>	$65^\circ < l < 175^\circ$ $-3.6^\circ < b < +5.6^\circ$	1'	1.32 km/s	3 K	32	108	256
SGPS <sup>b</sup>	$253^\circ < l < 358^\circ$ $-1.5^\circ < b < +1.5^\circ$	2'	1.0 km/s	1.6 K	30	42	54

<sup>a</sup>Data are available from <http://www2.cadc-ccda.hia-ihp.nrc-cnrc.gc.ca/cgps/>

<sup>b</sup>Data are available from <http://www.atnf.csiro.au/research/HI/sgps/queryForm.html>